Studies on shock interactions with moving cylinders using immersed boundary method

Kun Luo, Yujuan Luo, Tai Jin, and Jianren Fan*

State Key Laboratory of Clean Energy Utilization, Zhejiang University, Hangzhou 310027, People's Republic of China

(Received 10 October 2016; published 23 June 2017)

The process of shock interaction with a rigid cylinder is studied using a compressible immersed boundary method combined with a high-order weighted essentially nonoscillatory scheme. Movement of the cylinder is coupled to the flow field. First, the accuracy of the numerical scheme is validated. Then the influences of the incident shock Mach number and the cylinder diameter are discussed. The results are compared with those from cases with stationary cylinders. It is found that variation of either the incident shock Mach number or the cylinder diameter can cause different schlieren images. At a given dimensionless time, the trajectory of the upper triple point varies nonmonotonically with the incident shock Mach number while the primary reflected shock gets closer to the cylinder with increasing incident shock Mach number. For any moving case with a given incident shock Mach number and cylinder diameter, the trajectory of the upper triple point, the time evolution of the normalized vertical distance from the highest point of the primary reflected shock to the centerline of the cylinder, and the time evolution of the normalized shock detachment distance can all be predicted by linear correlation. As for the time evolution of the force exerted on the cylinder, the peak of the moving cylinder appears earlier than the stationary one in dimensionless time, with much lower value. Correlations to predict the occurrence of the peak drag and its value under different shock Mach numbers and cylinder diameters are proposed. The resulting cylinder movement is also briefly discussed.

DOI: 10.1103/PhysRevFluids.2.064302

I. INTRODUCTION

The interaction between shock and rigid bodies is a common phenomenon that may be involved in various practical occasions such as transdermal drug delivery [1] and particle burning in a solid rocket motor [2]. The dynamic process results in strong variation of both the flow field and the force exerted on the rigid bodies. Upon a shock the wave gets in touch with a rigid body, its front is modified, and the shock strength is reduced. During the interaction, reflected, refracted, and diffracted waves occur and various nonlinear waves such as Mach stems, contact discontinuities, and vortices may appear [3]. Meanwhile, the force exerted on the rigid body is quite unsteady [4–7]. The peak value is even an order of magnitude higher than that of the quasisteady force loaded on the rigid body when it is exposed to the steady flow field. Thus, the standard correlation for the quasisteady drag coefficient for a rigid body in compressible flow [8] cannot be applied to such a circumstance. Alternative models are required to correctly predict the variation of the drag force.

Such a problem has attracted a great deal of attention from many researchers for quite a long time [9–11]. Many relevant experimental studies have been conducted. The studies can mainly be divided into two types. One type is with a stationary obstacle, while the other type is with a moving obstacle. In the first type of study, the obstacle is fixed through different means and cannot move with the flow [12–16]. The size of the obstacle is relatively large and the transition from Mach reflection to regular reflection and the unsteady force exerted on the objects are of great interest. In the second type of study [17–19], due to the limit of the experiment, on the contrary, the object is

*Corresponding author: fanjr@zju.edu.cn

usually chosen to be very small, which makes the process during which the shock passes through the obstacle too short to be recorded. As a result, the interaction process cannot be studied in detail and the main focus can only be the variations after the interaction process. The object is assumed to be accelerated by uniform postshock gas flow that remains constant during the investigation and the quasisteady drag coefficient is often obtained from the obstacle's trajectory.

With the development of numerical methods and computational capability, the computational fluid dynamics has been an effective tool in solving problems that cannot be easily studied by experimental measurement. In recent years, the immersed boundary (IB) method [20] has gained popularity in the field of multiphase flow, in which the complexity of grid generation for complicated structures caused by the traditional grid conforming method [21–24] can be effectively avoided. It has been used to study the shock interaction with a stationary obstacle [25–27]. There also has been some progress on the shock interaction with moving boundaries. In the study of [28], the particles were forced to move with fixed velocities and directions, which is not suitable for the description of practical applications. In the study of [29], force on the obstacle was exerted by the surrounding fluid, but the authors just tested such a case to validate the proposed numerical scheme. In the study of [30], the authors studied the problem from the perspective of turbulence and were most concerned with the parameters related to the vortex. Among all these studies, the dynamics of shock-wave reflection have been scarcely investigated.

In the present study the dynamic interaction between shock and a rigid cylinder is studied. The problem is numerically simulated using a ghost-cell IB method coupled with the fifth-order weighted essentially nonoscillatory (WENO) scheme based on an inviscid approach. First, a ghost-cell IB method that allows us to simulate compressible flow with moving boundaries is proposed and its accuracy is verified and validated. Then the method is applied to study the shock interaction with a moving cylinder. The main objective of the present work is to investigate the dynamical influences on the flow field by the interaction process and the variation of the drag coefficient. The influences of the shock Mach number and cylinder diameter on the shock reflection trajectory, the dynamic drag coefficient, and the cylinder movement are analyzed. Taking these two physical parameters into consideration, correlations to predict the occurrence of the peak drag and its value are proposed. The overall differences between processes of shock interaction with a moving cylinder and a stationary cylinder are also discussed.

The paper is organized as follows. In Sec. II the physical model and numerical methods are presented, including the problem configuration, numerical scheme, and the ghost-cell immersed boundary method. Section III shows various numerical results for the shock interaction with a moving cylinder. First, results are compared with those in the literature to assess the capability of the proposed solver for handling moving boundary problems. Then the influences of two physical parameters (the incident shock Mach number and the cylinder diameter) on shock reflection trajectory, dynamic drag coefficient, and the cylinder movement are evaluated. We summarize in Sec. IV.

II. PROBLEM SETUP AND NUMERICAL METHODS

A. Problem configuration

In order to save computational resources, the problem is simplified to be two dimensional. Figure 1 shows a schematic illustration of the problem. The streamwise direction is designated as the x direction and the vertical direction naturally becomes the y direction. Initially, a cylinder with diameter D lies at the center of the computational domain with zero velocity and a planar shock wave (incident shock) is located upstream of it and propagates downstream along the x direction at a speed u_{si}. Postshock flow-field variables are denoted by the subscript L, while the subscript R is used for preshock flow. The Mach number of the incident shock is denoted by M_s and is defined as u_{si}/c_R, with c_R the sound speed in the preshock flow.

Typical inflow boundary conditions are used at the inlet in the x direction. The velocity, density, and temperature are specified, while the pressure is obtained by solving the equation of state for an

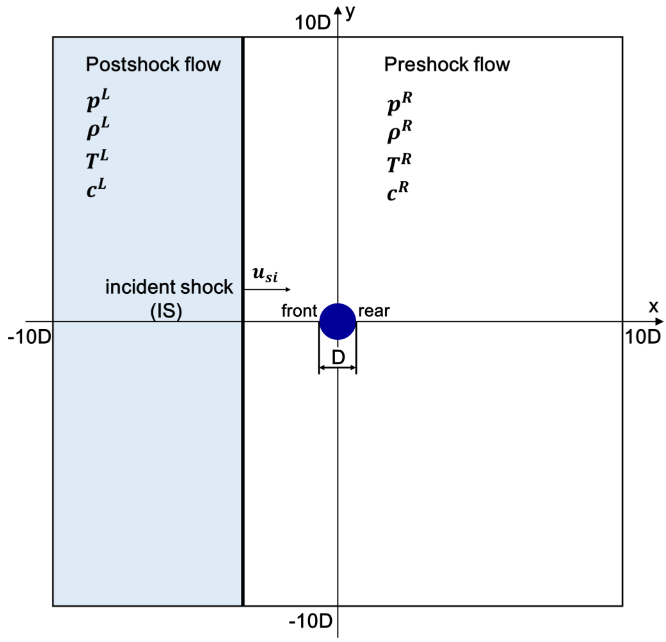

FIG. 1. Schematic illustration of shock interaction with a cylinder.

ideal gas. At the outlet, the partially nonreflecting Navier-Stokes characteristic boundary conditions proposed in [31] are imposed. Slip boundary conditions are applied at the transverse boundaries. On the surface of the cylinder, slip, no-penetration, adiabatic boundary conditions are assumed. Rankine-Hugoniot relations are used to connect the initial state of the preshock flow and the postshock flow.

B. Numerical scheme

Since the reflected shock wave is the major focus of the present study, the Euler equation for nonreactive compressible flows is utilized in the present study, following previous practice [32,33]. Its two-dimensional (2D) conservative form can be expressed as

$$\frac{\partial}{\partial t}\mathbf{u} + \frac{\partial}{\partial x}\mathbf{f}_1(\mathbf{u}) + \frac{\partial}{\partial y}\mathbf{f}_2(\mathbf{u}) = 0, \tag{1}$$

where $\mathbf{f}_1 = \begin{bmatrix} \rho u \\ \rho u^2 + p \\ \rho u v \\ u(E+p) \end{bmatrix}$, $\mathbf{f}_2 = \begin{bmatrix} \rho v \\ \rho u v \\ \rho v^2 + p \\ v(E+p) \end{bmatrix}$, and $\mathbf{u} = \begin{bmatrix} \rho \\ \rho u \\ \rho v \\ E \end{bmatrix}$. Here ρ is the density, u is the velocity in the x direction, v is the velocity in the y direction, p is the pressure, and E is the total energy. To close the system of equations, the equation of state for ideal gas is used here

$$p = \rho RT = (\gamma - 1)[E - \rho(u^2 + v^2)/2], \tag{2}$$

where T is the temperature of the fluid, R is the universal gas constant, and γ is the specific heat ratio (1.4 for air).

For a moving body, its motion is coupled to the solution of the flow. The body is assumed to be rigid without deformation. Its movement is then determined by the Newton-Euler equations

$$M^b \frac{d\mathbf{v}^b}{dt} = \mathbf{F}^b, \quad \frac{d\mathbf{x}^b}{dt} = \mathbf{v}^b, \quad \frac{d\mathbf{h}^b}{dt} = \mathbf{T}^b, \tag{3}$$

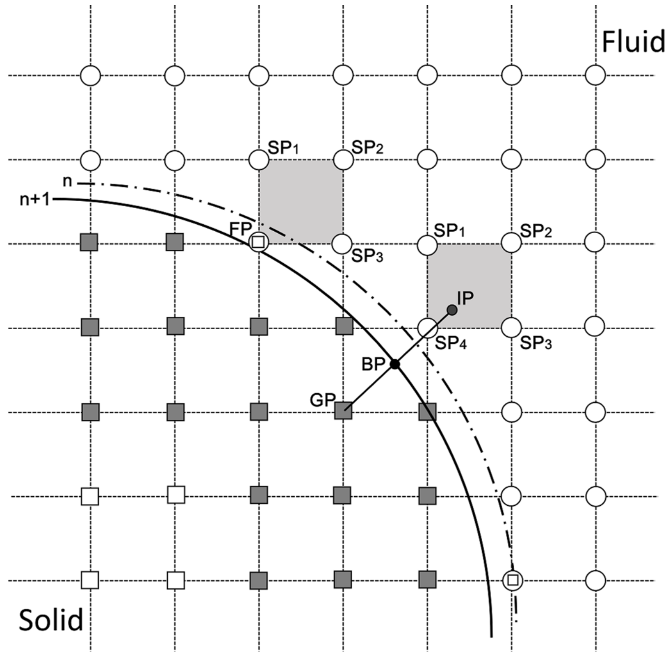

FIG. 2. Illustration of the present ghost-cell immersed boundary method.

where the first two equations describe the translation of the body, while the last one describes its rotation about the center of mass. Here M^b is the mass of the rigid body; $\mathbf{x}^b$ and $\mathbf{v}^b$ are the position and the velocity of the center of mass, respectively, which are both functions of time; and $\mathbf{F}^b$ is the surface force exerted on the body by the surrounding fluid. Since the flow is treated as inviscid, pressure becomes the only contribution to the total drag force $\mathbf{F}^b$. In addition, $\mathbf{h}^b$ is the angular momentum about the center of mass and $\mathbf{T}^b$ is the resultant torque.

Since strong discontinuity appears in the flow field, spatial discretization of the convective terms in the Euler equations (1) is implemented by using the fifth-order WENO scheme proposed by Jiang and Shu [34]. Compared to other Godunov class of high-resolution methods such as the monotonic upstream centered scheme for conservation laws and the essentially nonoscillatory scheme, it has many outstanding advantages. For example, it allows for higher-order accuracy in the interpolation of the interface variables [35]. Time advancement for flow-field variables and variables related to the motion of the boundary is performed simultaneously by the third-order Runge-Kutta total variation diminishing scheme [36].

C. Treatment of the immersed boundary

The ghost-cell immersed boundary method is used to enforce proper boundary conditions on the solid-gas interface. The method is based on the research of Mohd-Yusof [37] and Fadlun *et al.* [38]. The immersed boundary is treated as a sharp interface and no explicit addition of discrete forces to the governing equations is needed. The boundary condition is achieved through the use of ghost points, which act as stencil points for discretization of the flow field. To avoid numerical instability, an auxiliary point called an image point (IP) is introduced for each ghost point (GP), as shown in Fig. 2. Generally speaking, IPs do not necessarily coincide with grid points, so the flow properties at IPs are obtained by interpolation from its neighboring grid nodes.

It is usually more difficult to deal with a moving boundary than a stationary boundary. Many existing applications of the ghost-cell IB method for solving moving boundary problems are limited in the regime of incompressible flow [39,40]. In the present study, we extend the ghost-cell IB method for compressible flow. Compared to a stationary boundary, there are two more challenges when a moving boundary is considered. First, it is necessary to update the location of the interface and redefine all grid nodes every time step. Furthermore, a "fresh point" may appear. Fresh points (FPs) refer to grid points that are in the solid at the nth time step and become fluid points at the $(n+1)$th time step due to the motion of the boundary, as depicted in Fig. 2. For these points, values of $\partial \mathbf{f}_1(\mathbf{u})/\partial x$ and $\partial \mathbf{f}_2(\mathbf{u})/\partial y$ at the nth time step are unavailable and flow-field variables at the $(n+1)$th time step are usually obtained by interpolating from its neighboring grid points.

To get flow variables at IPs and FPs, the inverse distance weighting (IDW) interpolation scheme [27] is employed. At each IP, flow variables are obtained through interpolation from the surrounding four grid points and this interpolation procedure is similar for each FP. However, for a FP, one of the interpolation points is the FP itself, so little modification is needed. Three neighboring grid points are used for interpolation. Specific locations of stencil points (SPs) for interpolations of IPs and FPs can also be found in Fig. 2.

For clarification, the detailed implementation of the ghost-cell immersed boundary method in compressible flow can be summarized as follows:

(i) Construct the shape of the obstacle through an unstructured surface mesh [39]. For 2D cases, the boundary can be represented by many micro line segments.

(ii) Detect the interface between the solid and the fluid. Classify grid points into fluid points and solid points based on the two vertices and one normal vector of every surface element. At the same time, find the FPs among the fluid points.

(iii) Determine GPs and find boundary intercept points (BPs) as well as the corresponding image point (IP). In the present study, at least three layers of GPs are required for a complete computational stencil since the fifth-order WENO scheme is used for spatial discretization. Boundary intercept points are points that lie both at the boundary and at the edge of a probe that extends from a ghost point in the direction normal to the boundary. A schematic illustration of these points is shown in Fig. 2.

(iv) Obtain flow properties at FPs through IDW interpolation from neighboring grid points.

(v) Calculate flow-field variables such as velocity and density at IPs through interpolation from its neighboring grid nodes.

(vi) Update flow-field variables at GPs by incorporating values at their corresponding IPs and the prescribed boundary conditions at BPs.

III. RESULTS AND DISCUSSION

In this section the results from the shock interaction with a moving cylinder are presented. First, numerical validations are performed. Then the influences of the shock Mach number M_s and the cylinder diameter D on the flow structure and the drag force exerted on the cylinder are studied. Numerical simulations with different M_s (1.16, 1.28, 1.34, 1.5, 1.7, 2.0, 2.4, and 2.81) have been conducted with D maintained at 10 mm and the mass at 0.005 kg. To study the influence of D, three different diameters are chosen, 10, 15, and 20 mm, while M_s remains 1.16 and the mass remains 0.005 kg. Dimensionless time is defined as $t_r = u_{si}t/D$, where physical time $t = 0$ corresponds to the instant when the incident shock gets in touch with the very front of the cylinder.

The initial conditions for preshock flow are assumed to be $p = 0.05$ MPa and $\rho = 0.581\,32\ \mathrm{kg/m^3}$. The computational domain is chosen as $20D \times 20D$ to avoid wave reflections from outer boundaries and the grid size is chosen as $h = 1/160D$ based on the grid convergence test, which will be introduced later. Parallel computing is utilized in the present investigation and each case requires about 7 CPU h for 1 dimensionless time unit on 64 AMD Opteron$^{\mathrm{TM}}$ processors.

A. Numerical validation

1. *Piston problem*

To test the code's capability in solving moving boundary problems, the classical one-dimensional piston problem is considered. There are two main reasons to choose this example. First, the theoretical

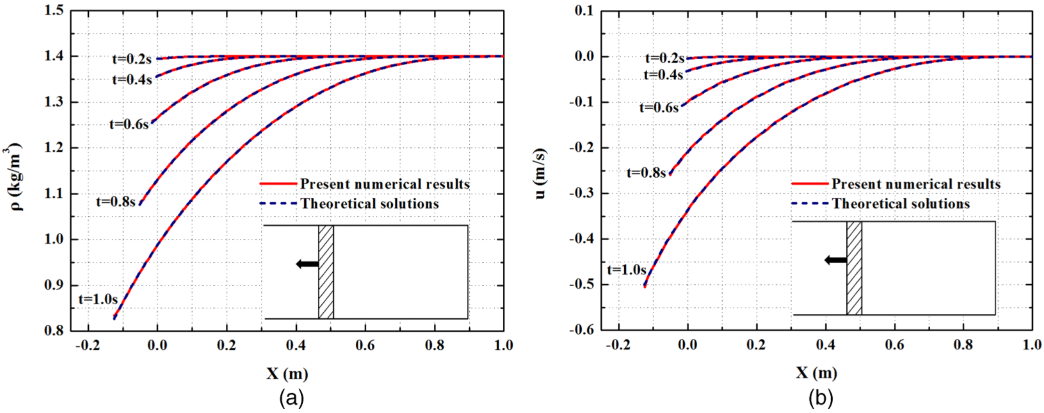

FIG. 3. Results for the one-dimensional piston problem: (a) density distribution and (b) velocity distribution.

solutions are available. Second, it is a good case to test the conservation property of the current numerical method. Initially, the space right to the piston is occupied by an ideal gas. The motion of the piston is described by a known function $x = g(t)$ for $t > 0$. If $\dot{g}(t) < 0$ and $\ddot{g}(t) < 0$, an exact solution can be constructed using the method of characteristics since no shocks form. Readers can refer to [41] for more details.

In our test the piston movement is specified by the function $g(t) = -t^4/8$ whose exact solution has two continuous derivatives. The computational domain is set to be [–0.75 m, 1.5 m] in the x direction (The solution does not depend on the y direction, so parameters in the y direction are relatively unimportant.) At $t = 0$, the surface of the piston lies at $x = 0$ and the state of the undisturbed flow on the right is set as $\gamma = 1.4$, $\rho = 1.4\,\mathrm{kg/m^3}$, $u_0 = 0\,\mathrm{m/s}$, and $p_0 = 1$ Pa. General profiles of the density and velocity distribution at different times are shown in Fig. 3 with a grid number of 400 in the x direction. The numerical results show good agreement with the theoretical solution.

For moving boundaries, conservation is always a great concern. It should be pointed out that the present numerical methods are not assumed to be strictly conservative. We have estimated the mass loss or gain on different resolutions with grid numbers of 100, 200, and 400 in the x direction, respectively. The mass loss of Δm is adopted to indicate the variation, whose definition is

$$\Delta m = \frac{\left|\sum_i \rho_i^{\text{final}}|C_i| - \sum_i \rho_i^{\text{initial}}|C_i|\right|}{\sum_i \rho_i^{\text{initial}}|C_i|}, \tag{4}$$

where C_i is a measure of the volume of the computational cell. For cells that are not cut by the surface of the piston, it is set as Δx. For the cell cut by the piston, it is chosen as the distance between the surface and the nearest grid point to the right.

Table I lists the mass error at $t = 1$ s. The mass loss decreases with increasing mesh solutions. From the table we can also see that the averaged global accuracy of the present numerical scheme is higher than second order.

TABLE I. Numerical error analysis for the piston problem.

Grid number	Δm	$O(\Delta x^n)$ global
100	1.63×10^{-3}	
200	2.87×10^{-4}	2.51
400	7.36×10^{-5}	1.96
average		2.24

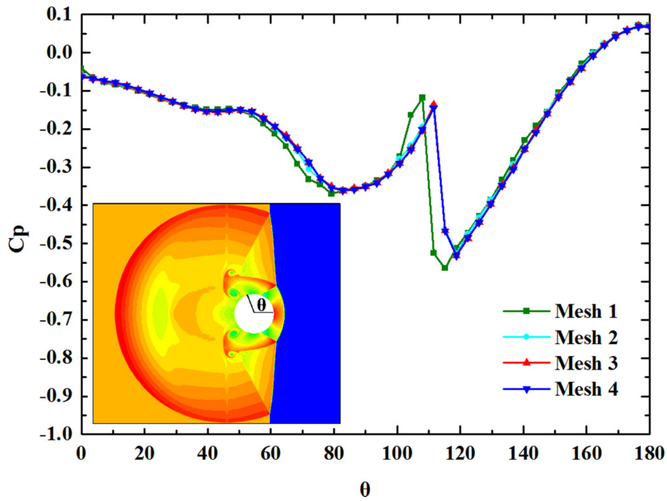

FIG. 4. Surface pressure coefficient under different mesh resolutions for a moving cylinder with $M_s = 2.81$.

2. *Moving cylinder problem*

In this section we test cases in which the motion of the object is determined by the surface stress exerted on it by the fluid. To check the grid dependence, we have implemented simulations with different grid resolutions for the case with $M_s = 2.81$ since it is the maximum shock Mach number in the present study that needs the finest grid resolution. Four different resolutions are tested: $h = 1/80D$ for mesh 1, $h = 1/160D$ for mesh 2, $h = 1/240D$ for mesh 3, and $h = 1/320D$ for mesh 4. Figure 4 shows the comparison of the computed surface pressure coefficient at $t_r = 4$ for different mesh resolutions. It is clear that the grid-independent solution can be achieved for a resolution of $h = 1/160D$. For convenience, this mesh resolution is used for all moving cylinder cases hereafter.

The resulting norms of relative errors computed on different meshes are depicted in Fig. 5. The local L_1 and L_2 norms are calculated based on the surface pressure coefficient C_p at $t_r = 4$ when the shock has passed the cylinder for some distance. One can conclude that the present IB method for a moving boundary exhibits an accuracy of second order.

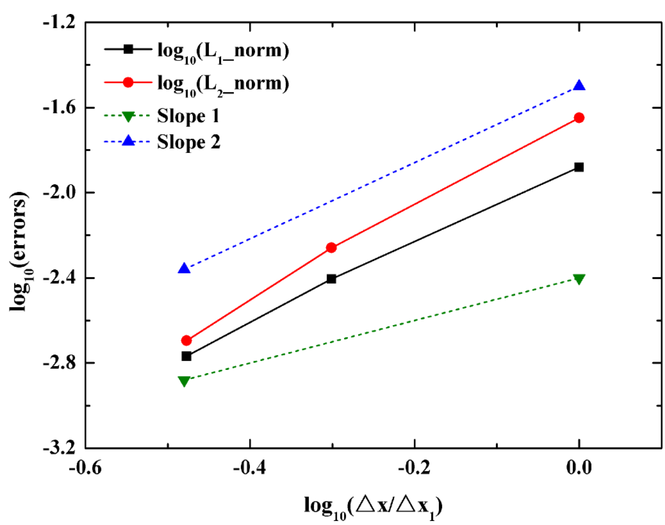

FIG. 5. Local norms based on the surface pressure coefficient (Δx_1 is chosen as the grid size of mesh 1).

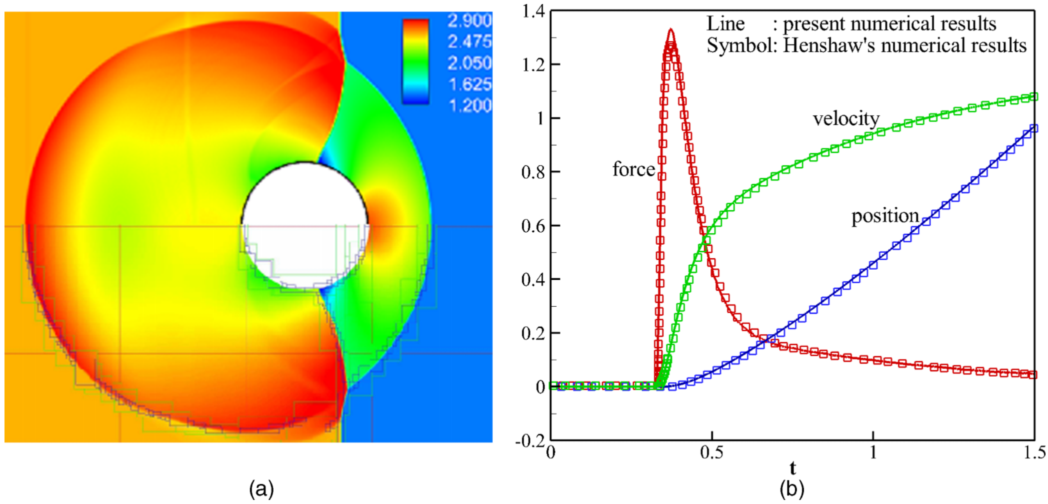

FIG. 6. Results for the moving cylinder with $M_s = 1.5$: (a) density contour at $t = 1.5$ s (top, present numerical result; bottom, numerical result from [29]) and (b) variation of the cylinder position and velocity and the force acting on it.

Furthermore, the moving cylinder problem with $M_s = 1.5$ [29,42] is investigated using the present methodology. The cylinder moves forward driven by the incident shock. The same initial and boundary conditions as well as computational domain setup as those of previous studies [29,42] are maintained for a complete comparison.

Figure 6 shows the results with a grid resolution of $h = 1/160D$. Figure 6(a) is the density contour at $t = 1.5$ s. Although a bow shock is also formed ahead of the cylinder, the flow structure within the bow shock shows very different characteristics compared with that of stationary cases. For stationary cylinders, contours stretched from the front part of the cylinder converge at the bow shock. However, in moving cylinder cases, contours stretched from the front part of the cylinder return to the surface of the cylinder itself. As the cylinder moves forward under the drive of the shock wave, a compression wave forms in the preshock flow. The postshock flow near the reflected bow shock is somewhat affected by it. Furthermore, the shape of the Mach stem may be modified due to the presence of the compression wave. By comparison, we can see that the present numerical results are in overall good agreement with those of [29].

The position and velocity of the center of mass as well as the drag force acting on the cylinder are shown in Fig. 6(b). Except for the little overestimation for the drag force for a short time duration near the occurrence of the peak drag, the comparison with numerical results in the studies of [42] and [29] is generally satisfactory.

B. Influences of incident shock Mach number M_s

In this section the influence of the incident shock Mach number M_s on the process of shock interaction with a moving cylinder is presented. The discussion mainly contains three aspects. One is the investigation of the flow structure that includes the flow field, the trajectory of the upper triple point (TP), the time evolution of the shock detachment distance X_R, and the vertical distance from the highest point of the first reflected shock to the centerline of the rigid body, which is denoted by Y_R. The other two include the analysis of the variation of the dynamic drag coefficient C_d and the cylinder movement. Due to the symmetry of the flow structure, when studying parameters related with flow structure such as the trajectory of the TP, the time evolution of X_R and Y_R, only the top half of the computational domain is presented in the paper. To illustrate the variation of TPs X_R, Y_R, and C_d, they are all normalized by D. In addition, the results are compared with those computed from cases where the cylinder remains stationary. Such rules also apply in Sec. III C.

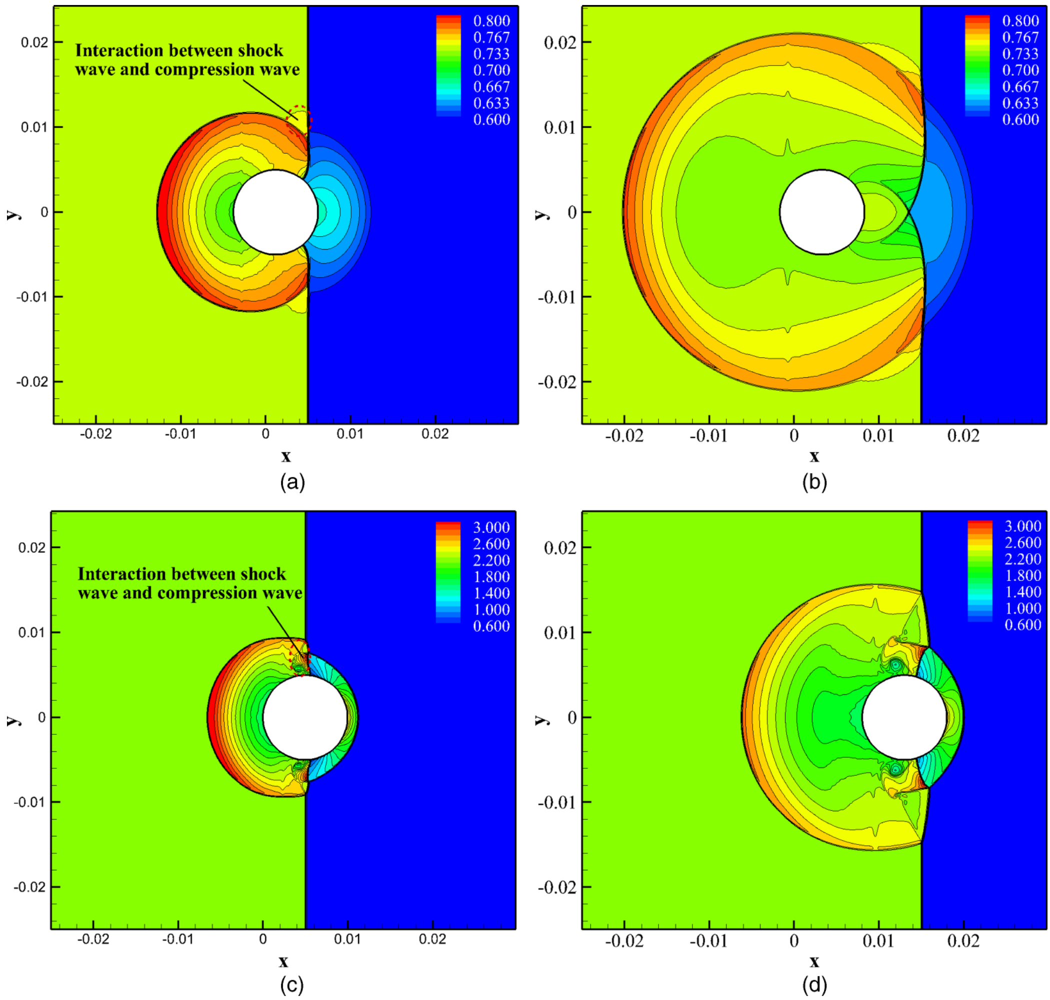

FIG. 7. Time evolution of the density field for a moving cylinder: (a) $M_s = 1.16$ and $t_r = 1$, (b) $M_s = 1.16$ and $t_r = 2$, (c) $M_s = 2.81$ and $t_r = 1$, and (d) $M_s = 2.81$ and $t_r = 2$.

1. Flow structure

Figure 7 shows the time evolution of the density field for cases of $M_s = 1.16$ and 2.81 at $t_r = 1$ and 2, respectively. Different features are observed for different M_s. For all cases, the area with the highest density (with the deepest red color in the contour) in the whole flow field lies near the front of the bow shock. The area shrinks with increasing M_s and it evolves into a very thin layer near the bow shock for the case of $M_s = 2.81$. The interaction between the shock wave and the compression wave caused by the motion of the cylinder leads to a very complex process. When the incident shock is weak, e.g., $M_s = 1.16$, the area of the compression wave is large enough to have an influence on the bow shock near the TP. With increasing M_s, the area becomes smaller and the affected region is transferred inside the bow shock where a complicated flow structure happens. Taking the case of $M_s = 2.81$, for example, a new high-density area forms near the intersection of the Mach stem and the compression wave. In addition, the strength of the compression wave has the same trend of variability as M_s. When the incident shock wave is strong enough, the compression wave even evolves into another new shock wave to form a very complicated wave system, as can be seen in the case of $M_s = 2.81$.

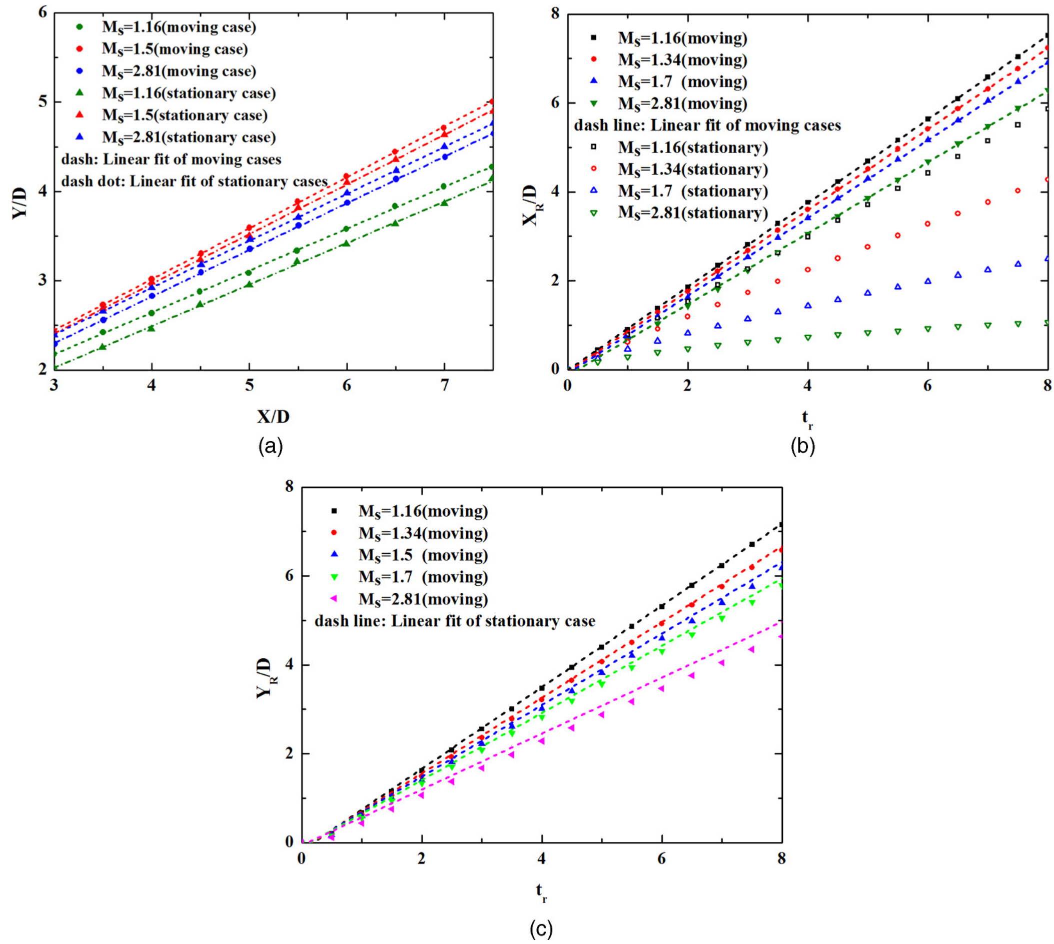

FIG. 8. Flow-field results for cases with different M_s: (a) trajectories of TPs, (b) time evolution of normalized X_R, and (c) time evolution of normalized Y_R.

When the cylinder moves, it is hard to figure out the real location of the TP when the upper shock system gets distorted by the compression wave. For this reason, paths of the TP after $t_r = 3.0$ are used for further analysis. The triple point's movements are recorded relative to the fixed origin of the coordinates. Figure 8(a) presents the trajectory of the TP for both moving and stationary cases with $M_s = 1.16$, 1.5, and 2.81. For both cases, we can see that at a given dimensionless time, the influence of M_s on the TP trajectory is not monotonic. When the shock is weak, its component in the y direction first increases with M_s. However, after reaching a critical M_s, it decreases with further increasing M_s. For a moving case with given M_s, it is found that the linear correlation is suitable to describe the trajectory of the TP (the minimum R^2 for the linear fitting is 0.9992), which is also true in stationary cases. It is interesting to find that when comparing the trajectories of moving cylinders to those of stationary cylinders, different trends are shown for different M_s. For $M_s = 1.16-1.7$, movement of the cylinder causes the path of the TP to lie a little higher than the fitting curve for the stationary cylinder and the amplitude decreases with increasing M_s, which results in a narrower gap between different cases especially for $M_s = 1.34-1.7$. In contrast, for $M_s = 2.81$, the opposite feature has been observed. As a result, the path of the case $M_s = 2.81$ is beneath that of $M_s = 1.28$.

The shock detachment distance X_R refers to the distance from the front of the reflected shock wave to the leading edge of the cylinder along the x axis. Variation of normalized X_R under different

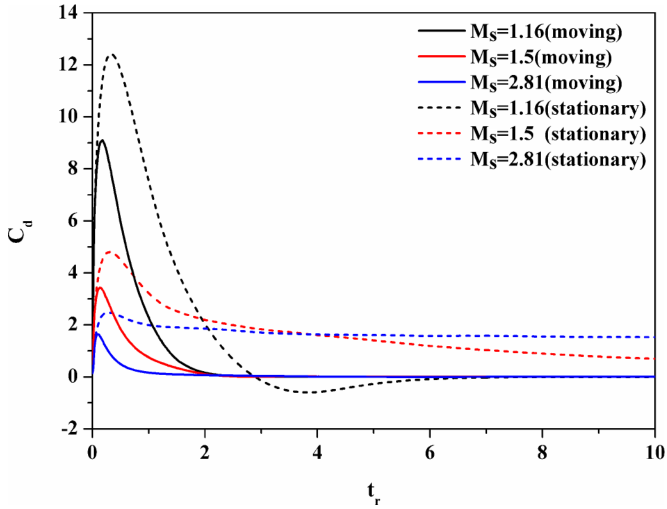

FIG. 9. History of the drag coefficient C_d for cases with different M_s.

M_s in both the moving and stationary cases is shown in Fig. 8(b). It is easy to see that at a given dimensionless time, the location of the front of the reflected shock wave gets closer to the front of the cylinder. Such a trend can be seen in both cases. However, the discrepancies produced by the variation in M_s shrink evidently in moving cases. For any moving case with given M_s, linear regression seems to be appropriate to approximate the time evolution of the normalized shock detachment distance (minimum R^2 for linear fitting increases to 0.9997). This is different from the stationary cases where the linear feature is only reserved in cases with weak incident shock.

At a given dimensionless time, a negative influence of M_s on normalized Y_R is observable in moving cases. For any moving case with given M_s, a linear feature is observed, with a minimum R^2 up to 0.9999. These two features can also be found in stationary cases. Actually, whether the cylinder moves or remains stationary has little influence on the history of normalized Y_R, especially when the incident shock is very weak, as can be seen in Fig. 8(c). For example, when $M_s = 1.16$, nearly no difference can be observed from the two cases. Only for larger M_s do discrepancies become more apparent.

2. History of the dynamic drag coefficient C_d

The dynamic drag coefficient is defined as $C_d = F_d/0.5\rho_L u_L^2 D$. Figure 9 shows the history of the drag coefficient C_d for cases with different M_s. The overall maximum drag values of moving cylinders are lower than those of stationary cylinders with earlier occurrence. Such a phenomenon can be attributed to the reduction of the relative motion between the shock and the cylinder. More notable differences between moving and stationary cases are observed for smaller M_s. For moving cylinders, after the descending stage, the drag immediately converges to a constant without the negative valley observed in cases with a stationary cylinder even for cases with small M_s. The difference in time when drag force begins to converge to a stable value under different M_s for moving cases is much less noticeable compared with stationary cases. Due to the earlier occurrence of the peak and quicker transition to the stable value, the whole dynamic process becomes much shorter when the cylinder is moving.

Since the interaction process is highly unsteady, it is of interest to find a correlation to predict the value and the occurrence of the drag peak. To obtain a full correlation for the maximum drag coefficient with different M_s and D, the method of separation of variables is applied. First, only the effect of M_s is considered in this part. Then the effect of D will be incorporated in the next section.

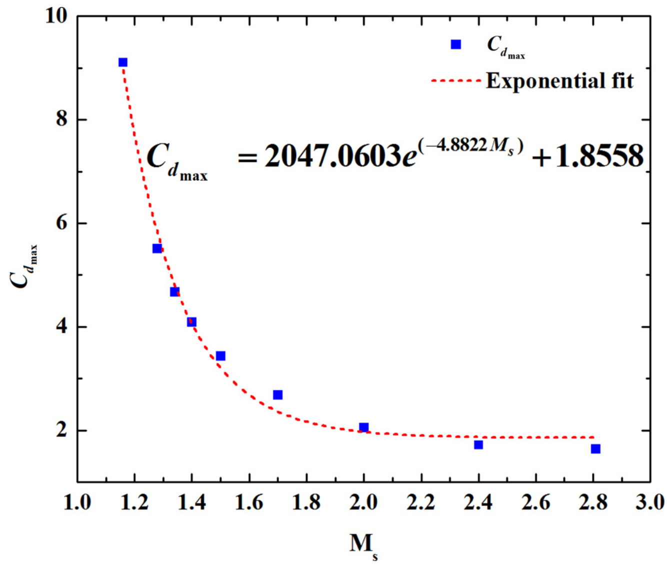

FIG. 10. Maximum C_d and exponential regression for a moving cylinder under different M_s.

The maximum C_d against M_s is plotted in Fig. 10. The scatters can be well fitted using the following exponential relation:

$$C_{d_{max}} = 2047.0603e^{-4.8822M_s} + 1.8558. \quad (5)$$

The different occurrence time against M_s is summarized in Fig. 11. A piecewise feature can be observed. For weak shock with $M_s = 1.16-1.4$ and $M_s = 1.4-1.5$, the occurrence of the maximum drag can be regarded as varying linearly with M_s. However, for larger M_s, it varies more smoothly with M_s and the linear assumption is not applicable under such a circumstance.

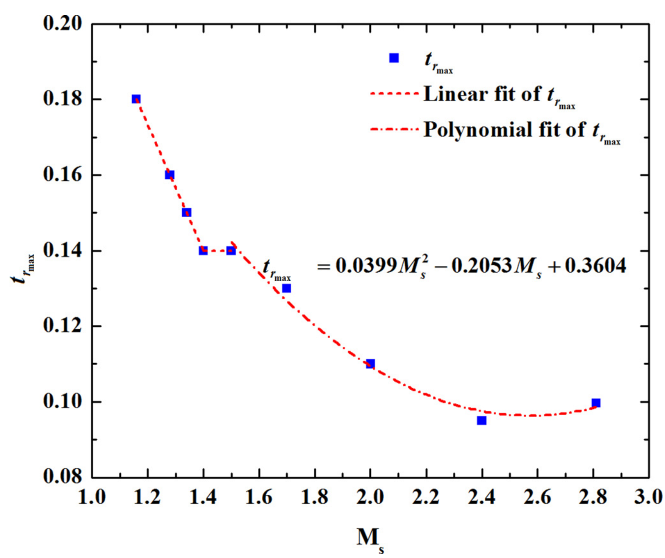

FIG. 11. Occurrence time of maximum C_d for a moving cylinder under different M_s.

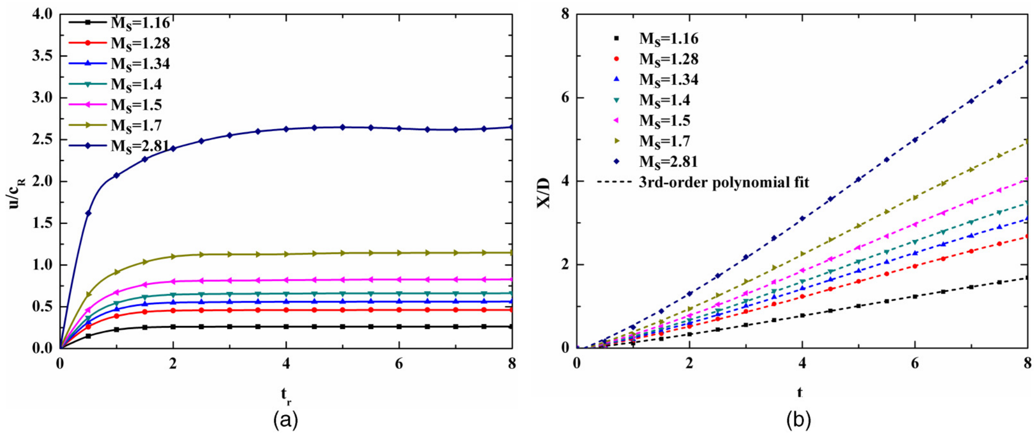

FIG. 12. Plot of (a) the x component of the velocity and (b) displacements in the x direction and third-order polynomial fittings.

3. Cylinder movement

As a result of the unsteady drag force, the cylinder accelerates rapidly, with velocity increasing from zero to a relative high value immediately when the shock hits the front of it. Some time after the shock has passed, the cylinder maintains a relative constant velocity to the postshock flow.

The influence of M_s on the cylinder velocity is plotted in Fig. 12(a). The cylinder velocity is normalized by sonic speed c_R in the preshock flow. Only cylinder movement in the x direction is taken into account since the incident shock moves in the x direction and cylinder displacement in the y direction is nearly nondetectable. When a stronger shock interacts with the cylinder, the acceleration process tends to be longer with a higher steady-state velocity. In most cases, the cylinder velocity approaches a subsonic value smoothly. However, for a strong shock such as $M_s = 2.81$, the cylinder velocity becomes supersonic in the postshock flow and little oscillation can be found even at a later stage during the investigated time. This indicates that the postshock flow becomes more unstable when M_s is large to a certain extent.

Based on the variation of cylinder velocity, the cylinder trajectory is thought to be able to be reconstructed using third-order polynomial fitting (the minimum R^2 is 0.9992). Shown in Fig. 12(b) is the time series of the cylinder location and its corresponding regression. Good agreement affirms our analysis, which is consistent with the conclusion drawn in [17].

C. Influence of cylinder diameter D

1. History of the dynamic drag coefficient C_d

When changing the cylinder diameter, the flow structure does not change much. However, D becomes an important factor contributing to the variation of C_d when the cylinder is driven by the incident shock, as can be seen in Fig. 13. Here C_d reaches a maximum value of 9.1068, 8.3164, and 7.7033 at $t_r = 0.18$, 0.13, and 0.13 for $D = 10$, 15, and 20 mm, respectively. It is clear that the maximum drag comes earlier for a larger cylinder with a higher value. Furthermore, a steady state can be achieved faster when increasing D.

For moving cylinders, both D and M_s have effects on C_d. The relation between maximum C_d and M_s has been obtained through Eq. (5). Here we conduct a further investigation about the influence of D. In Eq. (5) the value of D is set equal to 10 mm. Thus, $D = 10$ mm is taken as the base case. Here we use D_b to represent 10 mm. The ratio of the maximum C_d to that of the base case is denoted by C_{dr}. Through various attempt, we find polynomial regression to be the best fit for the relation

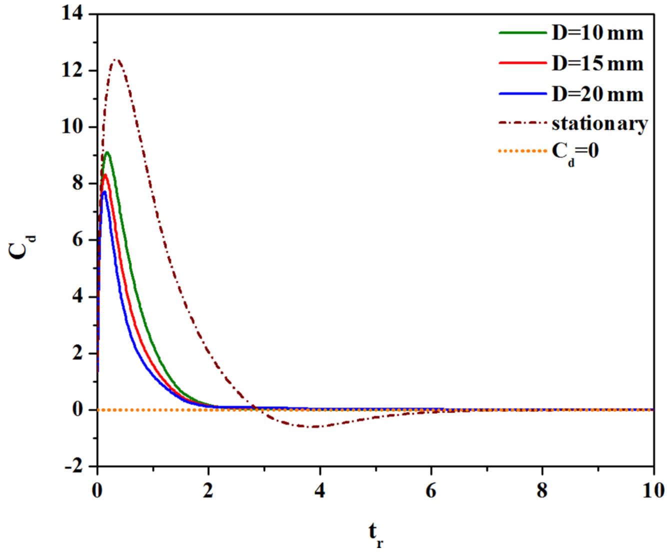

FIG. 13. History of the drag coefficient C_d for cases with different D.

between C_{dr} and D:

$$C_{dr} = 0.0390 \times \left(\frac{D}{D_b}\right)^2 - 0.2710 \times \frac{D}{D_b} + 1.2320 \tag{6}$$

Thus, taking M_s and D into consideration, the correlation to predict the maximum C_d for a moving cylinder under different M_s can be expressed as

$$C_{d_{\max}} = (2047.0603e^{-4.8822M_s} + 1.8558) \times \left[0.0390 \times \left(\frac{D}{D_b}\right)^2 - 0.2710 \times \frac{D}{D_b} + 1.2320\right]. \tag{7}$$

The influence of D is included only considering the case with $M_s = 1.16$. We also test other cases to prove its dependability. Table II shows comparisons between simulated results and solutions from Eq. (7) for various cases. The maximum error is within 10%. Good agreement validates the proposed correlation.

TABLE II. Comparisons between simulation and correlation results.

M_s	D (mm)	$\text{Cd}_{\max 1}$ (simulation)	$\text{Cd}_{\max 2}$ (correlation)	Relative error (%)
1.34	10	4.6692	4.8064	2.939
1.34	15	4.2631	4.3895	2.964
1.34	20	3.9482	4.0662	2.989
2.0	10	2.0550	1.9734	–3.970
2.0	15	1.8654	1.8022	–3.386
2.0	20	1.7335	1.6695	–3.691
2.8	10	1.7184	1.8582	8.14
2.8	15	1.5652	1.6970	8.42
2.8	20	1.4486	1.5720	8.52

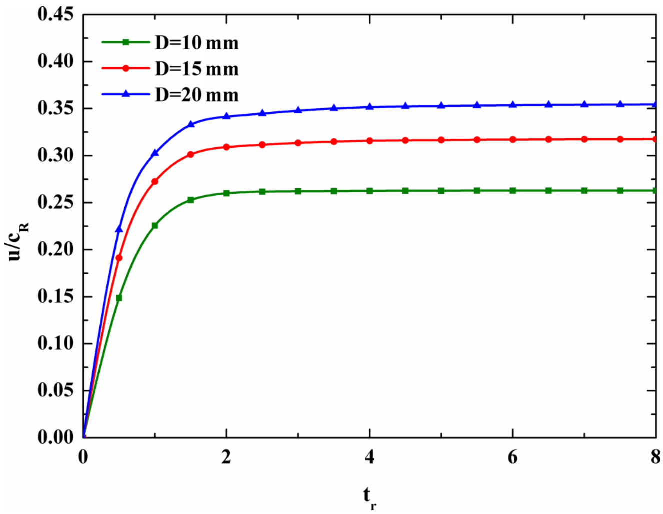

FIG. 14. Plot of the x component of the velocity for different D.

2. *Cylinder movement*

As for cylinder movement, a larger cylinder accelerates faster in the flow, as can be seen in Fig. 14. Although the states of the postshock flow remain the same for the three cases and the drag coefficient decreases with increasing D, the total drag force exerted on the cylinder actually grows with increasing D. This proves that variations in D cannot result in matched discrepancies in the total drag force. Generally speaking, in a case when the mass of the cylinder is fixed, we can make it larger to help it move and make it smaller to prevent its motion.

IV. CONCLUSION

In the present paper, the shock interaction with a moving cylinder was numerically studied. The numerical solver was based on the conjunction of the fifth-order WENO scheme and a ghost-cell immersed boundary method. The study intended to analyze the influences of the shock Mach number and cylinder diameter on the shock reflection trajectories, the dynamic drag coefficient, and the cylinder movement.

Both the shock Mach number M_s and cylinder diameter D have a strong effect on the interaction process. At a given dimensionless time, the trajectory of the TP varies nonmonotonically with M_s while both normalized X_R and normalized Y_R decrease with increasing M_s. For any moving case with given M_s and D, the trajectory of the TP, the time evolution of the normalized X_R, and the time evolution of the normalized Y_R can all be described using linear regression. This is very different from stationary cases. Details of the difference between moving and stationary cases have also been illustrated in the paper.

Besides the complex flow structure, we also investigated the variation of the dynamic drag coefficient C_d and the movement of the cylinder. Considering the effects of M_s and D, we proposed correlations to predict the peak drag coefficient. Although the application of the present correlation may be restricted, it reveals approximate trends how the maximum drag coefficient depends on parameters such as D and M_s, which is very helpful for further investigation to expand it to a broader range.

ACKNOWLEDGMENTS

This study was funded by the National Science Foundation of China (Grants No. 51576176 and No. 91541202) and the Fundamental Research Funds for the Central Universities (2016FZA4008). T. J. is also grateful for China Post-doctoral Science Foundation (2015M581928).

[1] Y. Liu, Performance studies of particle acceleration for transdermal drug delivery, Med. Bio. Eng. Comput. **44**, 551 (2006).
[2] J. C. Melcher, H. Krier, and R. L. Burton, Burning aluminum particles inside a laboratory-scale solid rocket motor, J. Propul. Power **18**, 631 (2002).
[3] See Supplemental Material at http://link.aps.org/supplemental/10.1103/PhysRevFluids.2.064302 for animations included.
[4] M. Parmar, A. Haselbacher, and S. Balachandar, On the unsteady inviscid force on cylinders and spheres in subcritical compressible flow, Philos. Trans. R. Soc. A **366**, 2161 (2008).
[5] M. Parmar, A. Haselbacher, and S. Balachandar, Modeling of the unsteady force for shock-particle interaction, Shock Waves **19**, 317 (2009).
[6] Y. Ling, A. Haselbacher, and S. Balachandar, Importance of unsteady contributions to force and heating for particles in compressible flows. Part 1: Modeling and analysis for shock-particle interaction, Int. J. Multiphase Flow **37**, 1026 (2011).
[7] Y. Ling, A. Haselbacher, and S. Balachandar, Importance of unsteady contributions to force and heating for particles in compressible flows. Part 2: Application to particle dispersal by blast waves, Int. J. Multiphase Flow **37**, 1013 (2011).
[8] M. Parmar, A. Haselbacher, and S. Balachandar, Improved drag correlation for spheres and application to shock-tube experiments, AIAA J. **48**, 1273 (2010).
[9] A. E. Bryson and R. W. F. Gross, Diffraction of strong shocks by cones, cylinders, and spheres, J. Fluid Mech. **10**, 1 (1961).
[10] W. H. Heilig, Diffraction of a shock wave by a cylinder, Phys. Fluids **12**, I154 (1969).
[11] J. Kaca, An interferometric investigation of the diffraction of a planar shock wave over a semicircular cylinder, UTIAS Technical Note 269, Institute for Aerospace Studies, University of Toronto, Canada, 1988.
[12] H. Tanno, K. Itoh, T. Saito, A. Abe, and K. Takayama, Interaction of a shock with a sphere suspended in a vertical shock tube, Shock Waves **13**, 191 (2003).
[13] M. Sun, T. Saito, K. Takayama, and H. Tanno, Unsteady drag on a sphere by shock wave loading, Shock Waves **14**, 3 (2005).
[14] K. Takayama and K. Itoh, in *Proceedings of the Fifteenth International Symposium on Shock Waves and Shock Tubes*, edited by R. H. Daniel Bershader (Stanford University Press, Berkeley, 1985), p. 479.
[15] B. W. Skews, M. S. Bredin, and M. Efune, Drag measurement in unsteady compressible flow. Part 2: Shock wave loading of spheres and cones, S. Afr. Inst. Mech. Eng. R&D J. **23**, 13 (2007).
[16] M. Geva, O. Ram, and O. Sadot, The non-stationary hysteresis phenomenon in shock wave reflections, J. Fluid Mech. **732**, R1 (2013).
[17] A. Britan, T. Elperin, O. Igra, and J. P. Jiang, Acceleration of a sphere behind planar shock-waves, Exp. Fluids **20**, 84 (1995).
[18] C. Devals, G. Jourdan, J. L. Estivalezes, E. E. Meshkov, and L. Houas, Shock tube spherical particle accelerating study for drag coefficient determination, Shock Waves **12**, 325 (2003).
[19] O. Igra and K. Takayama, Shock tube study of the drag coefficient of a sphere in a non-stationary flow, Proc. R. Soc. A **442**, 231 (1993).
[20] F. Sotiropoulos and X. Yang, Immersed boundary methods for simulating fluid-structure interaction, Prog. Aerosp. Sci. **65**, 1 (2014).
[21] A. Bagabir and D. Drikakis, Numerical experiments using high-resolution schemes for unsteady, inviscid, compressible flows, Comput. Meth. Appl. Mech. Eng. **193**, 4675 (2004).
[22] R. C. Ripley, F. S. Lien, and M. M. Yovanovich, Numerical simulation of shock diffraction on unstructured meshes, Comput. Fluids **35**, 1420 (2006).
[23] D. Drikakis, D. Ofengeim, E. Timofeev, and P. Voionovich, Computation of non-stationary shock-wave/cylinder interaction using adaptive-grid methods, J. Fluid Struct. **11**, 665 (1997).
[24] D. K. Ofengeim and D. Drikakis, Simulation of blast wave propagation over a cylinder, Shock Waves **7**, 305 (1997).
[25] H. Ji, F.-S. Lien, and E. Yee, Numerical simulation of detonation using an adaptive Cartesian cut-cell method combined with a cell-merging technique, Comput. Fluids **39**, 1041 (2010).

[26] E. Glazer, O. Sadot, A. Hadjadj, and A. Chaudhuri, Velocity scaling of a shock wave reflected off a circular cylinder, Phys. Rev. E **83**, 066317 (2011).
[27] A. Chaudhuri, A. Hadjadj, and A. Chinnayya, On the use of immersed boundary methods for shock/obstacle interactions, J. Comput. Phys. **230**, 1731 (2011).
[28] S. Takahashi, T. Nonomura, and K. Fukuda, A numerical scheme based on an immersed boundary method for compressible turbulent flows with shocks: Application to two-dimensional flows around cylinders, J. Appl. Math. **2014**, 252478 (2014).
[29] M. Balaji and M. Suresh, in *Proceedings of the 49th AIAA/ASME/SAE/ASEE Joint Propulsion Conference, San Jose, 2013* (AIAA, Reston, 2013), paper 2013-3655.
[30] M. Yusuke, T. Shun, N. Taku, N. Takayuki, and F. Kota, in *Proceedings of the 54th AIAA Aerospace Sciences Meeting, San Diego, 2016* (AIAA, Reston, 2016), paper 2016-0618.
[31] C. S. Yoo and H. G. Im, Characteristic boundary conditions for simulations of compressible reacting flows with multi-dimensional, viscous and reaction effects, Combust. Theor. Model. **11**, 259 (2007).
[32] I. N. Tsai, J.-C. Huang, S.-S. Tsai, and J. Y. Yang, Unsteady relativistic shock-wave diffraction by cylinders and spheres, Phys. Rev. E **85**, 026317 (2012).
[33] A. Bagabir and D. Drikakis, Mach number effects on shock-bubble interaction, Shock Waves **11**, 209 (2001).
[34] G. S. Jiang and C. W. Shu, Efficient implementation of weighted ENO schemes, J. Comput. Phys. **126**, 202 (1996).
[35] A. Mosedale and D. Drikakis, Assessment of very high order of accuracy in implicit LES models, J. Fluids Eng. **129**, 1497 (2007).
[36] C. W. Shu and S. Osher, Efficient implementation essentially non-oscillatory shock-capturing schemes, J. Comput. Phys. **77**, 439 (1988).
[37] J. Mohd-Yusof, Combined immersed-boundary/B-spline methods for simulations of flow in complex geometries, Annual Research Briefs, Center for Turbulence Research, NASA Ames and Stanford University, 1997, p. 317.
[38] E. A. Fadlun, R. Verzicco, P. Orlandi, and J. Mohd-Yusof, Combined immersed-boundary finite-difference methods for three-dimensional complex flow simulations, J. Comput. Phys. **161**, 35 (2000).
[39] R. Mittal, H. Dong, M. Bozkurttas, F. M. Najjar, A. Vargas, and A. von Loebbecke, A versatile sharp interface immersed boundary method for incompressible flows with complex boundaries, J. Comput. Phys. **227**, 4825 (2008).
[40] M. Shrivastava, A. Agrawal, and A. Sharma, A novel level set-based immersed-boundary method for CFD simulation of moving-boundary problems, Numer. Heat Transfer B **63**, 304 (2013).
[41] G. B. Whitham, *Linear and Nonlinear Waves* (Wiley, New York, 1974).
[42] W. D. Henshaw and D. W. Schwendeman, Moving overlapping grids with adaptive mesh refinement for high-speed reactive and non-reactive flow, J. Comput. Phys. **216**, 744 (2006).